XP-002412459

Structural Study of Mesoporous MCM-48 and Carbon Networks Synthesized in the Spaces of MCM-48 by Electron Crystallography

Mizue Kaneda,[†] Toshikazu Tsubakiyama,[†] Anna Carlsson,[†,§] Yasuhiro Sakamoto,[†]
Tetsu Ohsuna,[‡] and Osamu Terasaki[*,†,‖]

*Department of Physics, Tohoku University, Sendai 980-8578, Japan. Institute for Materials Science,
Tohoku University, Sendai 980-8578, Japan. and CREST, Japan Science and Technology Corporation, Japan*

Sang Hoon Joo and Ryong Ryoo

*National Creative Research Initiative Center for Functional Nanomaterials and Department of Chemistry
(School of Molecular Science-BK21), Korea Advanced Institute of Science and Technology,
Taejon 305-701, Korea*

Received: August 16, 2001; In Final Form: November 16, 2001

Recently, we have developed a new electron crystallography (EC) method for study of three dimensional (3D) structures of silica-mesoporous materials, and the 3D-structural solutions of MCM-48 and SBA-1, -6, and -16 were briefly reported. The method gives a unique structure solution through the Fourier sum of the 3D-structure factors, both amplitudes and phases, which are obtained from Fourier analyses of a set of high-resolution electron microscope (HREM) images. The method was fully described in an application for structure analyses of two MCM-48 crystals with different crystal morphologies. Little structural difference was observed between the two crystals, although small differences in the structure factors were observed. The space group of MCM-48 was determined to be Ia3d, and the wall surface of the two crystals followed exactly the periodic minimal surface of gyroid (G). The wall separated two interpenetrating and noninterconnecting channel systems with different chiralities. After structural analysis of MCM-48, the structures of two different carbon networks, CMK-1 and CMK-4, which were synthesized within the channels of MCM-48 from different carbon sources, were studied by electron microscopy (EM). It was observed that in both cases carbon networks were equally formed in the two channels of MCM-48 without changing the space-group symmetry and that the symmetry of Ia3d was retained after the dissolution of silica mesoporous MCM-48 for CMK-4 but changed to I4₁/a for CMK-1. The simplest model for structure change in CMK-1 was proposed on the basis of the observations of extra reflections in ED patterns and domain structures in HREM images as that the carbon networks equally formed in two noninterconnecting channels of MCM-48 were displaced during the dissolution relative to each other without rotation along the [001] axis by keeping each network rigidly. It is stressed that the method must be extended further for structural study of new materials with orders in two different lengths scales, atomic and mesoscopic scales.

Introduction

The MCM-48 ordered mesoporous silica is a member of the M41S silica family synthesized using surfactants as templates by Kresge et al.[1,2] The MCM-48 silica was claimed to have the cubic space-group symmetry of Ia3d (No. 230) because of the similarity in its powder X-ray diffraction (XRD) pattern with that reported previously for lipids[3] that belonged to the same space group as the periodic minimal surface of gyroid (G) discovered by Schoen.[4] All structural observations of the MCM-48 silica were explained well by assuming that the amorphous wall followed the G surface.[5–8] The silica MCM-48 was later

synthesized with crystal morphologies, and the crystallization process was studied by Ryoo et al.[9,10]

Recently, the structure of MCM-48 silica has been solved uniquely by electron crystallography (EC).[11] The main advantage of using the EC technique for mesoporous silica, compared to traditional X-ray single crystal diffraction, is that high-resolution electron microscope (HREM) images can be taken and that the phases of crystal structure factors (CSFs) are immediately available from the Fourier transform of the image. Another advantage is the orders-of-magnitude (approximately 10⁴) stronger interaction of electrons with matter compared with X-rays, which gives the possibility to use very small crystals down to only several tens of unit cells in size. These conditions allowed a data set to be obtained for three-dimensional (3D) CSFs from HREM images taken with several different zone axes and therefore a 3D structure in a straightforward way.[11,12] The EC result shows that the wall follows exactly the G surface with a thickness of ca. 13 Å and the wall separates the structure

* To whom correspondence should be addressed. E-mail: terasaki@
mup.phys.tohoku.ac.jp. Fax: +81-22-217-6475. Phone: +81-22-217-6472.
† Department of Physics, Tohoku University.
§ Present address: Haldor Topsøe A/S, DK-2800 Lyngby, Denmark.
‡ Institute for Materials Science, Tohoku University.
‖ CREST, Japan Science and Technology Corporation.

into two enantiomeric channel systems, which are not inter-connected with each other.[11] Because we can determine the 3D structure of mesoporous materials by EC now,[11,12] the silica mesoporous materials have attracted more attention as templates/containers for making new nanostructured materials within their spaces from their pore geometries.

The MCM-48 silica is suitable as a template (or mold) for the synthesis of new nanostructured materials that can attract much attention. For example, Ryoo et al. have demonstrated that carbonization of sucrose, furfuryl alcohol, and acetylene can be performed inside MCM-48 mesopores in a controlled fashion so that well-ordered mesoporous carbons can be obtained after the template is completely removed with HF or NaOH solution. They reported two different kinds of ordered meso-porous carbon, designated as CMK-1 and CMK-4, with MCM-48. The space-group symmetry of CMK-1 was reported to be $I4_{1}32$[13] and that of CMK-4 to be $Ia\bar{3}d$,[14] but detailed structural studies were left for further investigation. Such mesoporous carbons, constructed with ordered nanopores, are potentially of great technological interest for the development of advanced catalysts, sensors, and hydrogen storage systems. The nano-structured materials also attract much attention in fundamental science, because electrons confined in certain nanometer-scale geometries are likely to exhibit markedly different properties from bulk crystals due to an additional potential coming from the special geometry. Theoretically, this effect was claimed to be different from the quantum size effect.[15,16]

In the present work, we apply EC for an accurate structural study of two different crystals of MCM-48 with different crystal morphology, which were prepared in different conditions. Differences in the structural details of CMK-1 and CMK-4 were also studied by electron microscopy (EM). The result indicates that EM is a very powerful technique for the structural study of these materials.

Experimental Section

Samples. MCM-48 silicas were prepared in the "single crystal" form, following a hydrothermal synthesis procedure using aqueous solution of sodium silicate as the silica source, n-hexadecyltrimethylammonium bromide (HTABr) as the surf-actant, and ethanol (EtOH) as an additive for the meso-phase control. Briefly, the silica source was mixed with an aqueous solution containing the surfactant and ethanol at room temperature. The resulting gel mixture had a composition in the range of molar ratio 1.0 SiO_2/0.25 Na_2O/5 EtOH/0.65 HTABr/160 $\pm$ 40 H_2O. The gel mixture was heated in an autoclave at 413 K under static condition after being stirred for 1 h. The product obtained after an appropriate hydrothermal reaction time was filtered, washed with water, and dried in air at 823 K. The products were analyzed by X-ray powder diffraction and scanning electron microscopy as a function of the crystallization time to select a peak-quality sample corre-sponding to a given crystallization temperature. Two samples corresponding to the minimum (120 H_2O) and maximum (200 H_2O) water content were studied by EC. The crystallization times with 120 H_2O and 28 h with 200 H_2O These samples were designated as crystal-120 and crystal-200 re-spectively.

CMK-1 carbon was obtained following the synthesis method using sucrose as a carbon source.[5,17] Briefly, calcined MCM-48 silica was impregnated with sucrose solution in the presence of sulfuric acid. The resulting mixture was dried at 373 K and subsequently at 433 K, and then the impregnation/drying step
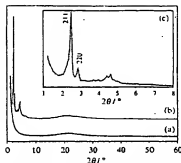

Figure 1. XRD powder patterns for fumed silica (a) and for MCM-48, crystal-120 (b). The expanded profile of panel b for small scattering angles is inserted as panel c.
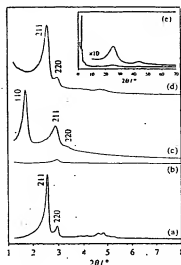

Figure 2. XRD powder patterns for MCM-48 (a), CMK-1/MCM-48 (b), CMK-1 (c), and CMK-4 (d). The profile of CMK-4 for large scattering angle is shown in panel c.

was repeated once. The obtained sample was carbonized under vacuum at 1173 K, and finally, the silica template was dissolved at 373 K in aqueous/ethanol solution of NaOH.

For the synthesis of CMK-4 carbon, as-synthesized MCM-48 silica was first converted to an aluminosilicate form with Si/Al = 20, following the postsynthesis incorporation proce-dure.[18] Briefly, the silica was washed with an ethanol−HCl mixture to remove the surfactant. The silica was dried in an oven at 413 K, impregnated with an aqueous solution of $AlCl_3$, dried at 413 K, and calcined in air at 813 K. The resulting mesoporous aluminosilicate template was heated to 1073 K in a fused quartz reactor through which acetylene gas was passed for 30 min at the flow rate of 200 cm^3 min^{-1}. After stopping the acetylene gas flow, the temperature was increased to 1173 K for 2 h under vacuum. The carbon/template composite thus obtained was washed with HF or NaOH solution to remove the template.

X-ray Powder Diffraction. Powder X-ray diffraction (XRD) patterns were recorded on Cu Kα (λ = 1.5406 Å) radiation operated at 40 kV and 55 mA (Philips X'Pen-MPD) in step scan mode (fixed time) with a small divergent slit and a graphite-counter monochromator. Powder XRD patterns of crystal-120 and crystal-200, both as synthesized and calcined, show almost
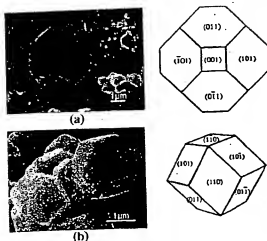
Figure 3. SEM images and schematic drawings of morphologies for crystal-120 (a) and crystal-200 (b).

the same pattern except for a small shift in peak positions. Therefore, the powder XRD pattern of crystal-120 as synthesized is shown in Figure 1b as a typical example, and that of fumed silica is shown in Figure 1a for comparison. A profile at small scattering angles is expanded and shown in Figure 1c. Diffuse maxima are observed at scattering angles of ca. 20° both in part a and in part b of Figure 1, and they are from short-range order in amorphous silica. All sharp diffraction peaks observed in MCM-48 crystals can be indexed by cubic system, and reflection conditions are consistent with the space-group symmetry of $Ia\bar{3}d$. Obtained lattice constants from the 220 peak position are as follows: crystal-120, 88 Å for as synthesized, 84 Å for calcined; crystal-200, 88 Å for as synthesized, 85 Å for calcined. MCM-48 crystals show reduction by ca. 4% in unit cell upon calcination.

This is clear from the comparison of the powder XRD patterns of MCM-48, CMK-1/MCM-48, CMK-1, and CMK-4, which are shown in Figure 2a–d. The XRD profile of CMK-4 for wide scattering angle range is shown in Figure 2e. The numbers of observed reflections and the diffraction peak intensity of CMK-1/MCM-48 are reduced substantially from that of MCM-48, but the existence of long-range order is clear. If all specimens are assumed to keep cubic symmetry, all diffraction peaks are indexed as indicated in the figures. Later, it will be made clear that CMK-1 appears cubic (i.e., accidentally $a = b = c$ and $\alpha = \beta = \gamma = \pi/2$ within our experimental resolution) but that the true symmetry of CMK-1 is tetragonal. Two characteristic features should be noted here for the figures: (i) only two weak peaks are observed in CMK-1/MCM-48 with a peak shift induced by lattice contraction and (ii) three peaks corresponding to lattice spacings of d_i (i = 1, 2, 3) = 51, 30, and 26 Å are observed in CMK-1. The ratio of them is given by $d_1:d_2:d_3 = 2\sqrt{3}:3:2:\sqrt{3}$, and therefore, they are indexed as 110, 211, and 220 on the basis of the result of the ED experiment, although 110 reflection is not allowed for $Ia\bar{3}d$ symmetry. Then, lattice constants are determined to be 74.5, 73.0, and 83.8 Å from the 211 peak position for CMK-1, CMK-1/MCM-48, and CMK-4, respectively.

Electron Microscopy. Scanning electron microscope (SEM) images were obtained with JEOL JSM-5400F with FEG at 1–3 kV. SEM images of crystal-120 and crystal-200 are shown in Figure 3a,b. The MCM-48s show "crystal morphology" as ordinary inorganic crystals do. The external surface of crystal-
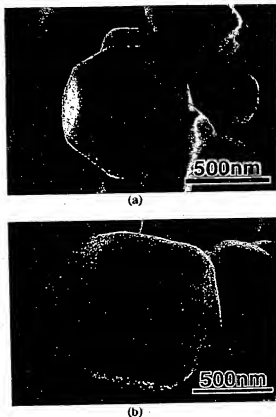

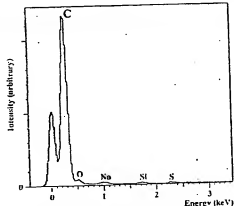Figure 4. SEM images of CMK-1/MCM-48 (a) and CMK-1 (b).

Figure 5. EDX profile of CMK-1. It is clear from the spectrum that silica MCM-48 is completely dissolved and that CMK-1 is almost pure carbon.

120 is bounded by six {100} and twelve {110} planes, and that of crystal-200 is bounded by twelve {111} planes. Both morphologies are commensurate with point group symmetry of cubic $m\bar{3}m$. Two typical crystal morphologies are well-known, that is, the equilibrium form determined by minimal surface energy (in equilibrium condition) and the growth form by anisotropy in growth rate (in nonequilibrium condition). It is a good case to study the two crystals by EC to find the difference in "mesocrystalline state" with high periodicity, because crystal-
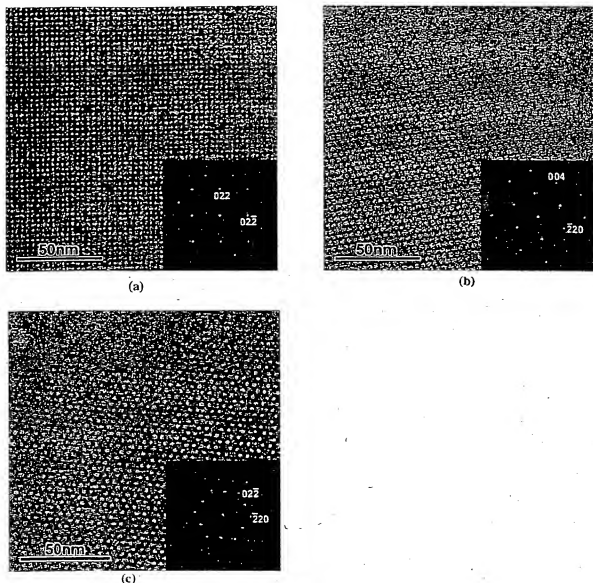
(a)

(b)

(c)

Figure 6. HREM images of crystal-120. Incident electrons are parallel with [100] (a), [110] (b), and [111] (c). Corresponding Fourier diffractograms (FDs) are inserted in each image.

120 may be formed under conditions closer to equilibrium than crystal-200 from a general sense in crystal growth.

The experimental observation, that both CMK-1/MCM-48 and CMK-1 show the same crystal morphology, which is similar to Figure 3b, as shown in Figure 4a,b, indicates the two following important points: (i) mesoporous MCM-48 takes a role as a template or a container, as carbons are formed inside the pore system of the crystal without serious damage of the mesoporous material and heavy precipitation on the external surface and (ii) carbon (CMK-1) can keep the same organization after dissolving the silica mesoporous MCM-48. The situation is also the same for CMK-4.

For transmission electron microscopy (TEM), the samples were investigated with a JEM-3010 operating at 300 kV (Cs = 0.6 mm, structural resolution 1.7 Å). Images were recorded with

TABLE 1: Number of Used HREM Images for MCM-48 Crystal Samples

samples	[100]	[110]	[111]	total
crystal-120 as synthesized	8	21	15	44
crystal-120 calcined	20	10	10	40
crystal-200 as synthesized	9	5	13	27
crystal-200 calcined	7	6	16	29

films and a CCD camera (model 794, Gatan, size 1024 × 1024, pixcel size 25 × 25 μm²) at 50 000—100 000 times magnification using low-dose conditions. Diffraction patterns were also recorded with both films and the CCD camera.

It was confirmed that all of the silica was dissolved completely by HF or NaOH solution for CMK-1 and CMK-4; energy-dispersive X-ray (EDX) analysis was performed in the

TABLE 2: A Summary of Observed 3D Crystal Structure Factors of MCM-48 Crystals for the Different Synthesis Conditions after Correction of CTF

h	k	l	sxs	d(Å)	crystal-120 as synthesized		crystal-120 calcined		crystal-200 as synthesized		crystal-200 calcined	
2	1	1	6	35.9	100.00	180°	100.00	180°	100.00	180°	100.00	180°
2	2	0	8	31.1	39.84	180°	41.68	180°	38.96	180°	49.19	180°
3	2	1	14	23.5	4.13	0°	5.31	0°	3.00	0°	4.88	0°
4	0	0	16	22.0	5.29	0°	9.67	0°	6.56	0°	8.24	0°
4	2	0	20	19.7	4.14	0°	4.56	0°	5.72	0°	4.73	0°
3	3	2	22	18.8	2.89	180°	6.48	180°	3.36	180°	5.99	180°
4	2	2	24	18.0	0.97	180°	2.21	180°	0.78	180°	1.72	180°
4	3	1	26	17.3	0.80	180°	0.60	180°	0.45	180°	0.76	180°
4	4	0	32	15.6	0.56	0°	0.53	0°	0.50	0°	0.89	0°
5	3	2	38	14.3	0.06	0°	0.16	0°	0.14	0°	0.16	0°
6	1	1	38	14.3	0.16	0°	0.82	0°			0.20	0°
6	2	0	40	13.9	0.11	180°	0.25	180°	0.07	180°	0.56	180°
5	4	1	42	13.6	0.14	0°	0.33	0°	0.14	0°	0.25	0°
4	4	4	48	12.7			0.31	180°	0.12	0°		
6	4	0	52	12.2	0.09	180°	0.12	180°	0.04	180°	0.37	180°
5	5	2	54	12.0			0.12	180°	0.05	180°	0.06	180°
6	3	3	54	12.0			0.14	0°			0.11	
6	4	2	56	11.8	0.08	0°	0.08	0°			0.05	0°
6	5	1	62	11.2	0.04	180°	0.01	180°			0.02	0°
8	0	0	64	11.0	0.08	0°	0.12	0°	0.06	0°	0.17	0°
8	2	0	68	10.7	0.04	0°	0.09	0°	0.03	0°	0.12	0°
6	6	0	72	10.4	0.07	180°	0.05	180°			0.08	180°
7	4	3	74	10.2			0.01	180°			0.01	0°
8	4	0	80	9.8		0°	0.03	180°	0.02		0.06	0°

TEM with Oxford LINK, ISIS 300. Figure 5 shows an EDX spectrum of CMK-1. The C Kα peak and almost no signal from Si were observed in the spectrum (C and Si are ca. 99.7 and 0.2 atom %, respectively), and the situation was the same for CMK-1.

Image Processing. Fourier transforms were obtained from the images taken of thin parts of the crystal. They are complex, in general, and their moduli as a function of wave vectors (in 2D k space) were displayed as Fourier diffractograms (FDs), from which extinction rules and hence space groups were determined. The transforms were corrected for the effect of the contrast transfer function (CTF) of the objective lens on the basis of weak-phase object approximation. The CTF affected both the amplitudes and the phases of the CSFs (diffraction peaks) in the Fourier transform. Amplitudes were dampened by multiplication with the value of the CTF, and when the CTF changed sign, there was a phase shift of π. Because of the rather low image resolution, an accurate determination of the defocus value from the zero crossings of the CTF could not be made. Most of the HREM images of mesoporous materials were taken at very under-focused conditions to obtain higher contrast. We have confirmed that the relative dependence of CTF on wavenumber in the range of $(10 \text{ Å})^{-1}$ at the focus conditions that we used is fairly independent of defocus values, so corrections were performed by applying the dependence of CTF on wavenumber at the Scherzer focus condition. Amplitudes and phases of diffraction peaks with a signal-to-noise ratio better than 3 were extracted from each Fourier transform. However, the phases showed the space-group symmetry only when the origin of the unit cell was chosen at the correct position, as required by the space-group symmetry. The correct position for the origin was found by moving the whole unit cell in small steps, imposing the symmetry, and comparing the symmetry-corrected phase values with the uncorrected ones. For most space groups, there are several possible origins. One of the points in the unit cell that gave the smallest difference between uncorrected and corrected phase values was selected as the correct phase origin. Even after the origin was moved to the correct place, the phases and amplitudes deviated slightly from those required by the symmetry for a number of reasons, such as random noise, beam tilt, and crystal tilt. After confirming the space-group symmetry, the symmetry of the space group

was therefore imposed on the amplitudes and phases. This averaging of symmetry-related amplitudes and phases further reduced the noise level, which was important for low-dose images such as these cases. All images were treated in a similar way with the symmetry of the respective projection imposed on the phases and amplitudes. Phases were carefully extracted by consulting several images and amplitudes from the highest quality image for each incidence. Reflections, which are common for the different projections, were used to scale the amplitudes and to check that the same origin had been chosen in all projections. Inverse Fourier transforms of the obtained structure factors gave the 3D- electrostatic potential map, that is, structure for the different samples.

Results and Discussion

1. MCM-48. It has been reported that, when MCM-48 is hydrothermally synthesized under the present experimental conditions, a disordered surfactant–silica mesostructure is first formed within a short period of the reaction time (ca. 2 h) and then transforms to very small MCM-48 particles, less than 0.5 μm in diameter. The MCM-48 particles increase in size continuously with time, reaching a crystal size of about 1–3 μm (ca. 18 h). After the crystal morphologies are maintained until 30 h of the reaction time, the crystals are dissolved and transformed rapidly to a lamellar mesophase that exhibits clusters of randomly curved leaf-like morphologies.[10]

Images taken with three different axes, [100], [110], and [111], were used for the structure analysis. The resolution for the analysis was limited to 10 Å, although some images showed a few higher-resolution spots. The unit cell of MCM-48 is ca. 90 Å, and subsequently, there were 34 unique reflections within this limit, that is, $h^2 + k^2 + l^2 < 80$. The numbers of images for different incidences used for collecting data are shown in Table 1.

Figure 6 shows HREM images taken from crystal-120 as synthesized with an incidence parallel to the [100], [110], and [111] directions, and corresponding FDs from the thin area are inserted. The FDs clearly show the condition for observable reflections: hkl, $h + k + l = 2n$; $0kl$, k and $l = 2n$; hhl, $2h + l = 4n$; $h00$, $h = 4n$. From these observations, the space-group symmetry was uniquely determined to be $Ia3d$.
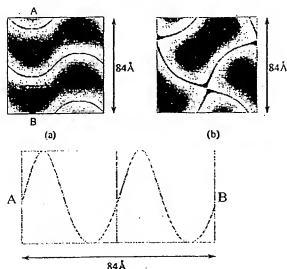
Figure 7. Electrostatic potential maps viewed along [100] at the sections of $z = 0$ (a) and $^1/_8$ (b) for crystal-120 (one unit cell). G surface sections are overwritten by solid curves. The section profile along the segment A–B is shown in panel c.

A summary of observed 3D crystal structure factors for the different synthesis conditions after correction of CTF is shown in Table 2. The reflections of 521, 631, 543, 721, 732, 741, 653, and 831 cannot be obtained from [100], [110], and [111] incidences. The 822 and 752 reflections are too small to be determined. But, it was confirmed through ED observations by tilting the crystal that the intensities of all of these reflections were very weak. The values for other vacant places in Table 2 were too small to be determined by the experiment ($S/N < 3$). The inverse Fourier transformations of observed 3D crystal structure factors were performed. Figure 7 shows the 3D electrostatic potential distribution maps at the section of $z = 0$ (a) and $z = ^1/_8$ (b), where origin was taken at the 3 point symmetry position (Wykoff notation 16a in International Tables for X-ray Crystallography, Vol. 4). By using periodic nodal function, the G surface is well described as $F(\mathbf{r}) = 0$, where $\mathbf{r} = (x,y,z)$ and $F(x,y,z) = \cos(2\pi x) \sin(2\pi y) + \cos(2\pi y) \sin(2\pi z) + \cos(2\pi z) \sin(2\pi x)$.[16]

The section of G surface is overwritten by solid curves in Figure 7a,b. and it is clear that the wall surface follows exactly the G surface. Figure 7c shows the potential at the section along the segment A–B in Figure 7a. To obtain the 3D structure, we must determine a threshold value in the potential density to give the boundary between the silica wall and the spaces for the materials synthesized in the spaces. Pore volumes were measured from N_2 gas adsorption for calcined crystal-120 and crystal-200 as 0.84 and 0.99 $cm^3 \ g^{-1}$, respectively. Assuming the density of the wall to be that of amorphous silica, 2.2 g cm^{-3}, the threshold in the 3D potential map is determined to be 197 and 205 in 256 gray scale for crystal-120 and crystal-200. The reconstructed 3D-structure model for crystal-120 is shown in Figure 8, parts a and b, which are a section of (100) and a 3D view along the [111] direction.

We can observe the difference in structure factors between the calcined crystal-120 and crystal-200, as shown in Table 2. Difference Fourier synthesis may be a method to indicate the difference after careful estimation of dynamical scattering effect. specimen thickness, and scaling in crystal structure factors.
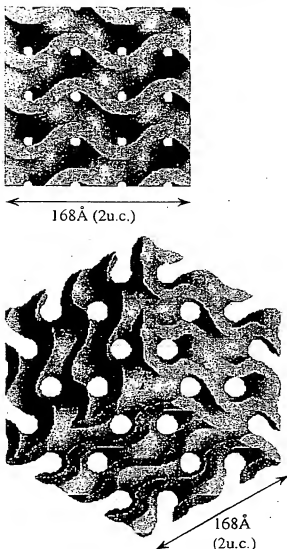
Figure 8. 3D reconstructed structure models: (a) (100) section; (b) 3D-view along the [111] (two unit cells).

The 3D structure shown in Figure 8 gives a clear boundary between the wall and the pores; however, those shown in Figure 7a–c give real structures of mesoporous materials including local fluctuation at the geometrical boundary. Therefore, it may be better to describe the 3D structure by that of Figure 8 together with a Gausian deviation parameter, which will be shown later. When the pores are occupied by surfactants or materials, we must find another way to evaluate threshold values in distinguishing boundaries between the silica wall and the surfactant or other materials in the pores because we cannot use gas adsorption data for the evaluation of pore volumes.

2. Carbon Networks, CMK-4 and CMK-1. a. CMK-4. HREM images of CMK-4 and corresponding FDs taken with [100]. [110]. and [111] directions are shown in Figure 9. The HREM image of CMK-4 shows that the carbon rods are composed of small graphical carbons as shown in Figure 10. From the FDs, the space group is uniquely determined to be $Ia\bar{3}d$. which is the same as that for MCM-48. The 3D structure

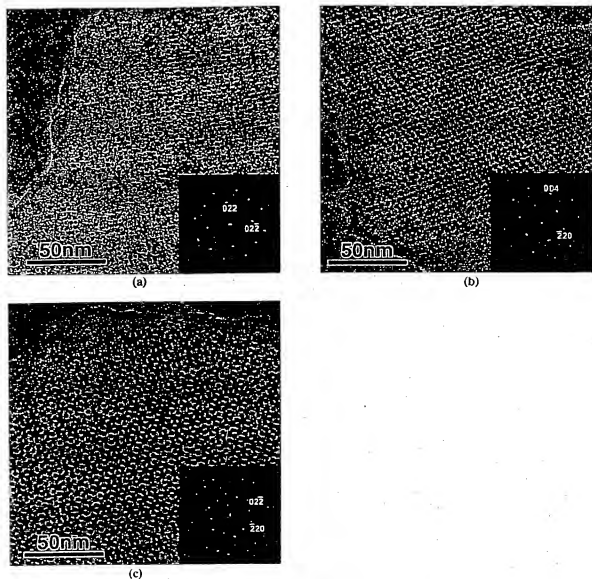(a)   (b)

(c)

Figure 9. HREM images of CMK-4. Incident electrons are parallel with [100] (a), [110] (b), and [111] (c). Corresponding Fourier diffractograms (FDs) are inserted in each image.

TABLE 3: Observed 3D Crystal Structure Factors of CMK-4 with Data of MCM-48 for Comparison

hkl	d (nm)	CMK-4		MCM-48	
		amp.	phase (deg)	amp.	phase (deg)
211	3.52	100.0	180	100.0	0
220	3.04	43.6	180	41.7	0
321	2.30	4.1	0	5.3	180
400	2.15	14.5	0	9.7	180
420	1.92	10.7	0	4.6	180
332	1.83	13.5	180	6.5	0
422	1.75	5.3	180	2.2	0
431	1.69	3.4	180	0.6	0

factor data were collected in the range of 17 Å^{-1}, and those for eight reflections were determined as shown in Table 3, in which the values for calcined crystal-120 are relisted for comparison.

It is to be noted that the phases of structure factors are exactly opposite to those for MCM-48. Pores of MCM-48, both right- and left-hand channel systems, are filled by carbon uniformly, and therefore, Babinet's principle is working out. Figure 11 shows the 3D potential density map for CMK-4 obtained by the same procedure as crystal-120 and crystal-200. The electrostatic potential density distribution is continuous, and this may come from local variation/fluctuation in MCM-48 of the boundary between the silica wall and the space. Pore volume was measured but could not be observed precisely from N$_2$ gas adsorption in this case because the amorphous carbon thin layer was formed on the external surface as small aggregates, which were confirmed by EM images.

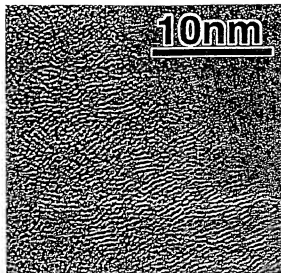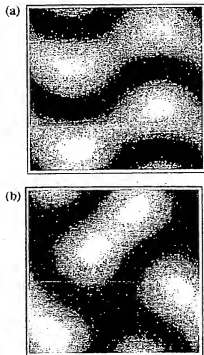To determine the 3D structure of CMK-4 without pore volume measurement, we must find another way to define the

Figure 10. HREM image of CMK-4.

Figure 11. 3D potential density map for CMK-4 viewed along [100] at the sections of $z = 0$ (a) and $1/8$ (b) (one unit cell).
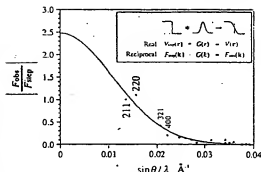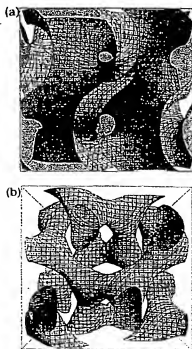

Figure 12. Schematic illustration showing relation between potential with step and that of observation by convolution of a Gaussian function, which gives local variation between the silica wall and the pores (surfactant molecules were there) in Real space (inset). Observed CSFs are well reproduced by this approach; $\sigma = 0.08$ was chosen.

Figure 13. 3D structure of CMK-4 (a). To show rod connectivity clearly, a thinner rod model is shown in panel b.

boundary between the silica wall and the pores. We assumed that local variation of the wall surface produces a smooth profile instead of a stepwise as the average structure and that local variation of CMK is the same as that of the MCM-48 crystal. By introducing one parameter, σ, which smoothes the boundary through a function $G(r)$, $G(r) = \exp[-r^2/(2\sigma^2)]/[\sigma(2\pi)^{1/2}]$ and is determined later to give a better fit between observed and calculated CSFs. This process is illustrated schematically in

Figure 12 in one dimension. Carbon is filled uniformly in the range of $\mathrm{abs}\{F(r)\} < 0.7$; then, in real space, potential distribution will be given by the step function $V(r)_{\mathrm{step}}$, and actual average potential distribution $V(r)$ is given by $V(r) = V(r)_{\mathrm{step}} * G(r)$, where $*$ indicates the convolution operation in Fourier mathematics. In reciprocal space, $F_{\mathrm{obs}}(k) = F_{\mathrm{step}}(k)G(k)$. The value of σ is estimated to be $\sigma = 0.08$ in the scale of the unit cell constant for MCM-48, where reflections up to 431 were used to build up V_{step} as shown in Figure 12. The same approach was tested for SBA-6, the structure of which we reported previously, and the value of σ is estimated to be $\sigma = 0.10$. Therefore, we may assume that this approach is useful and the value of σ falls in the range of 0.08–0.10.

Figure 13 shows the 3D structure of CMK-4, where σ is taken to be 0.08 as reasonable value. This gives 30 Å for the diameter
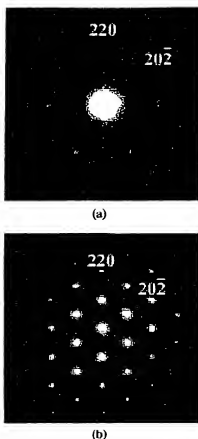
Figure 14. ED patterns of CMK-1/MCM-48 (a) and CMK-1 (b) taken with the [111]. The {110}-type reflections were clearly observed in panel b.

of carbon and ca. 35% for pore volume. If σ = 0.10 or 0.06 is taken, these value will be 28 Å and 30% or 32 Å and 40%, respectively.

b. CMK-1. The ED patterns taken with the [111] incidence are shown in Figure 14, parts a and b, for CMK-1/MCM-48 and CMK-1. ED patterns obtained from CMK-1/MCM-48 and CMK-1 can be indexed by the cubic system. It can be concluded that CMK-1/MCM-48 keeps the same symmetry, *Ia3̄d*, as MCM-48, although number of observed reflections is small. The {110}-type reflections, which are not allowed in *Ia3̄d*, are observed clearly in Figure 14b, and it is confirmed by tilting a crystal that the reflections are not produced by multiple scattering but are genuine. The HREM image of CMK-1 taken with the [111] and the corresponding FD are shown in Figure 15a,b. Threefold or sixfold (in projection) symmetry is hardly observed in the image, although the symmetry is nearly observed in the FD shown in Figure 15b. Figure 15, parts c, d, and e are filtered images formed by a set of {110}, {211}, and {220}, a set of {110} only, and a set of {110} and {211} reflections, respectively. Figure 15e shows almost *p6mm* symmetry; therefore, the deviation from threefold as seen in Figure 15a,c,d is not specimen tilting effect. The HREM image of CMK-1 taken with the [100] is shown in Figure 16 and the corresponding FD is shown in the inset. In Figure 15b, 004 is the only observed reflection for type 00*l*, and this indicates that there is 4₁
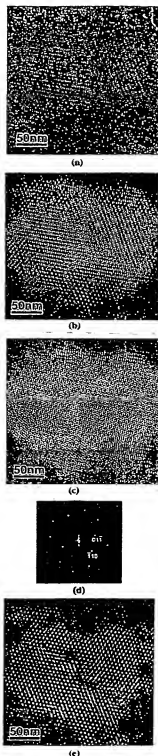

Figure 15. HREM image of CMK-1 taken with the [111] (a), corresponding FD (b), filtered images formed by a set of {110}, {211}, and {220} reflections (c), a set of {110} reflections only (d), and a set of {110} and {211} reflections (e).
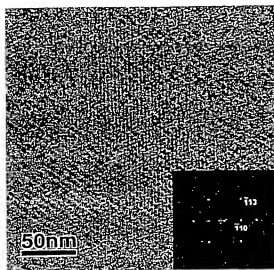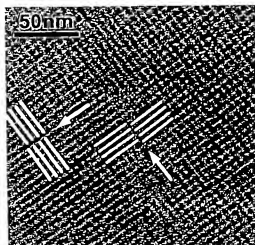
Figure 16. HREM image of CMK-1 taken with the {110} and corresponding Fourier diffractogram (inset).

symmetry along the c direction, which is a part of symmetry element of $Ia3d$.

Figure 17a,b shows the HREM image of [001] and its FD. By looking at the image along the several fringe directions, it is easy to recognize that the image has domain character. To show this clearly, lattice fringes, which correspond to the {110} type with spacing of $d_{110} = 52.7$ Å, are drawn in Figure 17a. In addition to the fact that CMK-1/MCM-48 shows $Ia3d$ symmetry as a composite, the characteristic features of the CMK-1 structure are summarized from the above observations as follows: (i) the symmetry is lower than cubic keeping 4_1 along the [001], that is, tetragonal; (ii) the crystal consists of small domains, and on average, over these domains it appears as cubic. This is because there are three possibilities with an equal possibility for the direction of the unique axis, that is, [100], [010], and [001] directions. The simplest model to give all of the above observations is the following displacement model: (i) carbon rods are equally formed in two noninter-connecting channels of MCM-48, and (ii) during dissolution of the silica wall, two carbon rods are displaced relative to each other without rotation along the [001] axis by keeping each rod rigidly, and the resultant space group is $I4_1/a$ (No. 88). This is confirmed by image simulations based on this model as shown in Figure 17c, if displacements are along [100] in region A, [010] in region B, and [010] in C region A. CMK-1 consists of a small domain with tetragonal, and as an average structure, this also explains an appearance of a cubic system in unit cell size. To explain the powder XRD and ED patterns, CSFs for several reflections were calculated as a function of magnitude for mutual displacement along the [100] based on this space group as shown in Figure 18. All {110}-type reflections, as an example, are degenerate if the crystal is cubic, but by this displacement along the [100], the crystal will be tetragonal and $1\bar{1}0$ reflection becomes nondegenerate from other 101 and $01\bar{1}$ reflections, which are still degenerate. From the figure, observations in the XRD profile and ED patterns are well explained by this model, especially for intensity enhancement for 110-type reflection, and our structural model is reasonable. To find tetragonality in unit cell size, we need to have high-resolution diffraction data of the XRD profile at large scattering vectors,

(a)

(b)
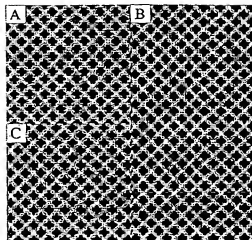
(c)

Figure 17. HREM image of CMK-1 taken with the [001] and (100) including lattice fringes drawn by lines (a) and corresponding Fourier diffractogram (b). To clarify, simulated images corresponding to panel a are shown in panel c by [110] lattice fringes.

and this seems to be very difficult because of strong damping in intensity with scattering angles.

EM is the most powerful and may be the only technique for solving these structures. We must extend the EM technique further for the ordered structure in two different lengths, that is, atomic and meso scales; because we have succeeded in synthesizing a novel 3D network of Pt nanowires in MCM-48.[19]
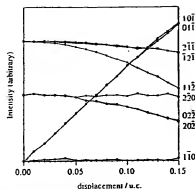
Figure 18. Dependence of structure factors for important reflections on the magnitude of the displacement.

References and Notes

(1) Kresge. C. T.; Leonowicz, M. E.; Roth. W. J.; Vartuli, J. C.; Beck, J. S. *Nature* 1992, *359*, 710–712.

(2) Beck, J. S.; Vartuli, J. C.; Roth, W. J.; Leonowicz, M. E.; Kresge, C. T.; Schmitt, K. D.; Chu, C. T.-W.; Olson, D. H.; Sheppard, E. W.; McCullen, S. B.; Higgins, J. B.; Schlenker, J. L. *J. Am. Chem. Soc.* 1992, *114*, 10834–10843.

(3) Luzzati. V.; Spegt. P. A. *Nature* 1967, *215*, 701–704.

(4) Schoen. A. H. NASA Technical Note D-5541; NASA: Washington, DC, 1970.

(5) Monnier. A.; Schuth. F.; Huo. Q.; Kumar, D.; Margolese, D.; Maxwell. R. S.; Stucky, G. D.; Krishnamurty. M.; Petroff. P.; Firouzi. A.; Janicke. M.; Chmelka. B. F. *Science* 1993, *261*, 1299.

(6) Schmidt. R.; Stocker. M.; Akporiaye, D.; Torstad, E. H.; Olsen, A. *Microporous Mater.* 1995, *5*, 1–7.

(7) Alfredsson. V.; Anderson, M. W. *Chem. Mater.* 1996, *8*, 1141–1146.

(8) Alfredsson. V.; Anderson. M. W.; Ohsuna, T.; Terasaki. O.; Jacob, M.; Bojrup, M. *Chem. Mater.* 1997, *9*, 2066–2070.

(9) Kim, J. M.; Kim, S. K.; Ryoo. R. *Chem. Commun.* 1998, 259–260.

(10) Ryoo, R.; Kim, J. M. In *Proceedings of the 12th International Zeolite Conference, Baltimore, MD, July 5–10, 1998;* Treacy. M. M. J., Marcus, B. K., Bisher, M. E., Higgins, J. B., Eds.; Materials Research Society: Warrendale, Pennsylvania, 1999; Vol. I, pp 689–696.

(11) Carlsson, A.; Kaneda, M.; Sakamoto, Y.; Terasaki, O.; Ryoo. R.; Joo, S. H. *J. Electron Microsc.* 1999, *48*, 795–798.

(12) Sakamoto, Y.; Kaneda, M.; Terasaki, O.; Zhao. D. Y.; Kim, J. M.; Stucky, G.; Shin, H. J.; Ryoo, R. *Nature* 2000, *408*, 449–453.

(13) Ryoo. R.; Joo, S. H.; Jun, S. *J. Phys. Chem. B* 1999, *103*, 7743–7746.

(14) Ryoo. R.; Joo, S. H.; Jun, S.; Tsubakiyama. T.; Terasaki, O. In *Zeolites and mesoporous materials at the dawn of the 21st century, Montpellier, France;* Galarneau, A., Di Renzo, F., Faujula. F. Vedrine, J., Eds.; Studies in Surface Science and Catalysis 135; Elsevier Science: Amsterdam, 2001.

(15) Jensen, H.; Koppe, H. *Ann. Phys.* 1971. *63*, 586–591.

(16) Itegami, M.; Nagaoka. Y. *Prog. Theor. Phys., Suppl.* 1991, *106*, 235–248.

(17) Ryoo, R.; Jun, S.; Kim, J. M.; Kim, M. J. *Chem. Commun.* 1998, 2225–2226.

(18) Joo, S. H.; Jun, S.; Ryoo, R. *Microporous Mesoporous Mater.* 2001, *44–45*, 153–158.

(19) Shin, H. J.; Ryoo. R.; Liu, Z.; Terasaki, O. *J. Am. Chem. Soc.* 2001, *123*, 1246–1247.